Control of Architecture in Rhombic Dodecahedral Pt–Ni Nanoframe Electrocatalysts

Nigel Becknell,[†,‡,¶] Yoonkook Son,[†,¶] Dohyung Kim,[§] Dongguo Li,[∥] Yi Yu,[†,∇] Zhiqiang Niu,[†] Teng Lei,[†] Brian T. Sneed,[⊥] Karren L. More,[⊥] Nenad M. Markovic,[∥] Vojislav R. Stamenkovic,*,[∥] and Peidong Yang*,[†,‡,§,#]

[†]Department of Chemistry, University of California, Berkeley, Berkeley, California 94720, United States
[‡]Materials Science Division, Lawrence Berkeley National Laboratory, Berkeley, California 94720, United States
[§]Department of Materials Science and Engineering, University of California, Berkeley, Berkeley, California 94720, United States
[∥]Materials Science Division, Argonne National Laboratory, Argonne, Illinois 60439, United States
[⊥]Center for Nanophase Materials Sciences, Oak Ridge National Laboratory, Oak Ridge, Tennessee 37831, United States
[#]Kavli Energy NanoSciences Institute, Berkeley, California 94720, United States

S *Supporting Information*

ABSTRACT: Platinum-based alloys are known to demonstrate advanced properties in electrochemical reactions that are relevant for proton exchange membrane fuel cells and electrolyzers. Further development of Pt alloy electrocatalysts relies on the design of architectures with highly active surfaces and optimized utilization of the expensive element, Pt. Here, we show that the three-dimensional Pt anisotropy of Pt–Ni rhombic dodecahedra can be tuned by controlling the ratio between Pt and Ni precursors such that either a completely hollow nanoframe or a new architecture, the excavated nanoframe, can be obtained. The excavated nanoframe showed ~10 times higher specific and ~6 times higher mass activity for the oxygen reduction reaction than Pt/C, and twice the mass activity of the hollow nanoframe. The high activity is attributed to enhanced Ni content in the near-surface region and the extended two-dimensional sheet structure within the nanoframe that minimizes the number of buried Pt sites.

The proton exchange membrane fuel cell (PEMFC) is a critical technology to enhance the clean, sustainable production and usage of energy for society, implementing hydrogen as the energy storage medium.[1] Hydrogen fuel for the PEMFC can be obtained by water electrolysis powered by a renewable energy source, completing the sustainable and carbon-free water cycle.[2,3] Initial applications of PEMFCs have been to replace the gasoline engine in powering personal vehicles.[4] A major roadblock preventing PEMFCs from increased infiltration into the transportation sector is the cost of the platinum-based catalysts that perform the oxygen reduction reaction (ORR) in the cathode.[1] Although Pt shows the highest catalytic activity among the elements of the periodic table, it is necessary to reduce the total amount of Pt within a PEMFC in order to be cost-competitive with gasoline powered vehicles.[5]

To improve the ORR reaction rate and lower Pt loading in the cathode, major efforts have been placed on the study of Pt alloys with cheap, 3d transition metals (M).[6−10] Pt−M nanocatalysts have demonstrated Pt-based mass activity that reaches the magnitude required to significantly reduce the cost of PEMFCs while maintaining performance. Nevertheless, improvements are still needed; specifically, discovering optimal spatial distributions of elements at both the atomic level and the nanoscale. Stamenkovic et al. have shown ORR activity enhancement by inducing surface atomic rearrangement to create Pt-skin structures in Pt−Ni alloys.[11−14] Pt-skin utilizes atomic scale segregation of Ni just beneath a pure Pt surface to tune the electronic structure of the surface. At the nanoscale, control over the elemental spatial distribution in bimetallic alloys can create unique nanoparticle architectures for ORR catalysis.[15,16] Finely controlled nanoparticle synthesis mechanisms such as nucleation, step-induced deposition, and atomic diffusion can create an anisotropic distribution of one element within a bimetallic nanoparticle.[17] In recent reports, Pt-rich edges could be formed in Pt−M rhombic dodecahedra that remained after corrosion of the M-rich interior, resulting in hollow Pt_3M nanoframes (NF).[8,18] Here, we demonstrate precise control of the Pt anisotropy in Pt−Ni rhombic dodecahedra, resulting in a NF that has a unique morphology with enhanced ORR activity.

Through control of the concentration and ratio of Pt and Ni precursors, thereby adjusting their chemical potentials, we have altered the three-dimensional elemental distributions in solid rhombic dodecahedra (SD) to create either only Pt-rich edges (Figure 1a) or Pt-rich edges together with Pt-rich sheets inside the SD (Figure 1b). The synthetic mechanism of the Pt−Ni SD was previously investigated and begins with the formation of Pt-rich branches around which step-induced Ni deposition occurs (Figure S1).[15] We discovered that at this stage, preferential deposition of Pt occurred when the Ni precursor concentration was lowered. The Pt was deposited between the
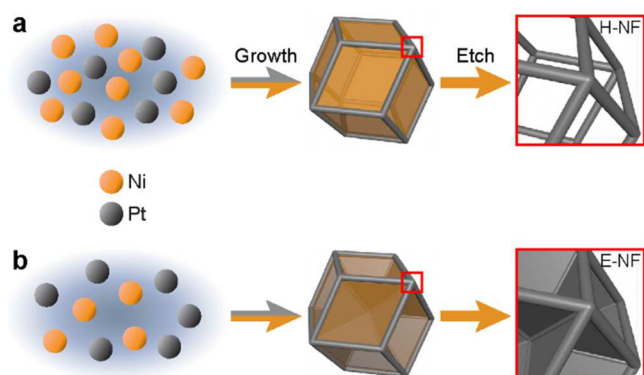
Figure 1. Illustration of the synthetic routes to create (a) hollow nanoframe (H-NF) and (b) excavated nanoframe (E-NF). In the models, orange represents Ni-rich regions and gray represents Pt-rich regions.

Pt-rich branches in addition to segregating to the edges and branches, resulting in Pt-rich sheets inside the SD. The sheets are bordered by both interior branches and exterior edges of the SD. Ni eventually deposited in the concave sites formed by the growing branches and sheets in order to fill out the SD. This synthetic control allowed us to obtain excavated nanoframes (E-NF) after a Ni corrosion step that contain not only Pt-rich edges, but also sheets extending inward from the edge of the NF. If we used high Ni concentration, hollow nanoframes (H-NF) similar in architecture to previous work were obtained.[8,13,15,18] Two major differences between the synthesis of SD in this work and previous work must be emphasized.[8] First, in this work, the precursors are dissolved in oleylamine before injection in order to maintain better control of the injection procedure. In the previous work, the precursor solution was aqueous. Second, the amount of Ni^{2+} precursor is adjusted in order to control the architecture of the resulting NF.

Figure 2a,b shows transmission electron microscopy (TEM) and scanning electron microscopy (SEM) images for H-NF that demonstrate its hollow interior. Though the SD precursors to H-NF and E-NF (H-SD and E-SD) exhibited similar morphology to each other (Figure S2), E-NF in Figure 2d,e displays sheet-like structures that remain after corrosion of Ni
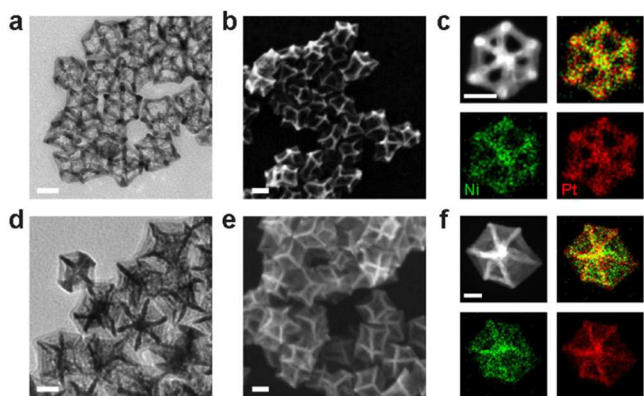

Figure 2. TEM and SEM images of (a, b) hollow nanoframe and (d, e) excavated nanoframe (scale bars represent 20 nm). STEM-HAADF image and STEM-EDS mapping of (c) hollow nanoframe and (f) excavated nanoframe oriented in the ⟨111⟩ direction (scale bars represent 10 nm).

due to their Pt-rich composition. Figure 2c,f shows high angle annular dark field (HAADF) scanning transmission electron microscopy (STEM) images and STEM-energy dispersive X-ray spectroscopy (EDS) mapping of H-NF and E-NF oriented in the ⟨111⟩ direction.[8] The lack of Pt and Ni signal inside H-NF is evident, whereas E-NF exhibited a uniform distribution of Pt and Ni throughout its structure.[19] Figure S3a shows STEM-EDS for E-NF in the ⟨110⟩ direction demonstrating sheet formation extending from edge to edge. Figure S3b,c shows dense and uniform Ni distribution in H-SD and E-SD, respectively, before Ni corrosion. Similar to the NF case, E-SD exhibited Pt distributed throughout the particle while Pt signal is stronger on the edges of H-SD.

Figure S4 compares powder X-ray diffraction (XRD) patterns of NFs and SDs, with all samples demonstrating face-centered cubic structures. The diffraction of NFs was symmetric due to their uniform composition, while SDs had asymmetric patterns because of segregation of Pt from Ni. Table 1 presents the compositions of SDs and NFs. Bulk

Table 1. Compositions of Solid Rhombic Dodecahedral Precursors to the Hollow and Excavated Nanoframes (H-SD and E-SD) and the Two Nanoframes (H-NF and E-NF)

	ICP	XPS
H-SD	Pt_9Ni_{91}	$Pt_{19}Ni_{81}$
E-SD	$Pt_{29}Ni_{71}$	$Pt_{32}Ni_{68}$
H-NF	$Pt_{67}Ni_{33}$	$Pt_{80}Ni_{20}$
E-NF	$Pt_{65}Ni_{35}$	$Pt_{73}Ni_{27}$

composition information was obtained from inductively coupled plasma optical emission spectroscopy (ICP-OES). Near-surface composition was estimated by X-ray photo-electron spectroscopy (XPS) measurements (Figure S5). Further explanation of the XRD data and the ICP and XPS comparison for SDs is provided in the Supporting Information.

The ICP and XPS compositions for H-NF and E-NF showed that both NFs had Pt-rich surfaces compared to their bulk compositions. However, H-NF exhibited more severe Pt enrichment on its surface. This is consistent with the original phase segregation patterns in H-SD and E-SD (Figure S6). XRD and STEM-EDS demonstrated that E-SD had less segregation of Pt from Ni in the form of the interior sheet structures. Therefore, it was expected and confirmed by XPS that after corrosion, E-NF had more Ni in the near-surface region than H-NF. E-NF also demonstrated a greater extent of alloying (J_{Pt} and J_{Ni}) compared to H-NF as measured by extended X-ray absorption fine structure (EXAFS) analysis (Figure S7, Table S1, see SI for additional details).[20] Because the sheet structure in E-NF has a larger Ni ratio in the near-surface region, Ni will influence the electronic structure of the catalyst surface to a greater degree than in H-NF. It is well-known that Pt−Ni alloys have a downshift in the surface d-band center position compared to pure Pt, leading to weaker binding with surface adsorbates and higher ORR activity.[6,11,21,22] In addition, the extended sheet structure of E-NF is likely to have fewer low-coordinated sites considering all surface atoms. EXAFS showed that the average coordination number of Pt in E-NF is higher than H-NF (Table S1), indicating that H-NF would have more low-coordinated sites that bind oxygenated adsorbates more strongly during ORR.[23] It is confirmed below that, as expected, both H-NF and E-NF have Pt-skeleton surface structure considering the Ni corrosion process used and

lack of high temperature annealing that would lead toward the Pt-skin structure.[6,11,12,14] However, because H-NF has a more Pt-rich surface with more low-coordinated sites than E-NF, we would expect it to bind adsorbates too strongly, resulting in lower specific activity for H-NF.

As discussed previously, in the formation process of Pt−Ni SD, a branched nanoparticle forms from the initial nucleated seed.[15] Under lower Ni concentration, as in the synthesis of E-SD, Pt could compete with Ni for deposition between the branches such that some Pt remains inside E-SD. After corrosion of Ni, the Pt that had deposited inside E-SD formed the sheet structure that is bound by the interior branches and exterior edges of E-NF. We established the most probable model for E-NF (Figure 3a) based on the mechanism of Pt−Ni

Figure 4. (a) Cyclic voltammograms recorded at room temperature in Ar-saturated 0.1 M $HClO_4$ solution with a sweep rate of 50 mV/s. (b) ORR polarization curves recorded at room temperature in O_2-saturated 0.1 M $HClO_4$ solution with a sweep rate of 20 mV/s and a rotation rate of 1600 rpm. (c) Specific activity and (d) mass activity at 0.95 V vs RHE for Pt/C, H-NF, and E-NF as compared to Pt_3Ni NFs with Pt-skin.[8]

Figure 3. (a) Model of E-NF shown in three orientations, where red indicates branches of type A and black indicates branches of type B. See Figure S1 for more details. (b) HRTEM image of E-NF oriented in ⟨110⟩ direction. The top left inset is the corresponding model of E-NF in the identical orientation. The bottom left inset is the FFT of the image in the red box. (c) Magnified HRTEM image of thin sheet in E-NF from green box in panel b, with high-tilt angle STEM tomography rendering of E-NF in inset. All scale bars represent 5 nm.

SD formation and the TEM and SEM images. To confirm the model, we performed high-resolution TEM (HRTEM) and high-tilt angle STEM tomography. Although most 2-D projections of this model contain two overlapping sheets, if the model E-NF is oriented in the ⟨110⟩ direction, a region exists where the electron beam must pass through only one sheet, as shown in Figure 3b. This image corresponds well with the model of E-NF oriented in the same direction (top left inset). The fast Fourier transform (FFT) of a single sheet (bottom left inset, taken from portion of image in red box) confirmed the ⟨110⟩ orientation. Figure 3c shows the high crystallinity of a single-sheet and a tomography rendering of E-NF, demonstrating the spatial distribution of the extended sheet structures more clearly in 3-D (see Movies S1 and S2 in SI).

We loaded the 3-D nanoframes on carbon support (Figure S8) to compare their ORR catalytic activity. H-NF and E-NF were elecrochemically tested using the rotating disk electrode method and benchmarked against a commercial Pt/C catalyst. The cyclic voltammograms in Figure 4a show the hydrogen underpotential deposition (H_{upd}) process used to measure the electrochemical surface area (ECSA). The ECSA was 60.2 m²/g_{Pt} for H-NF and 48.1 m²/g_{Pt} for E-NF, which are both less than that of commercial Pt/C (76.1 m²/g_{Pt}). As expected, the quasi-2D nature of E-NF meant that it had slightly lower ECSA than the quasi-1D H-NF. Electrooxidation of adsorbed CO provided similar ECSA to H_{upd} such that the ratio $ECSA_{CO}$/$ECSA_{Hupd}$ was found to be 1.03 for both electrocatalysts (Figure S9). This confirms that, due to the synthetic method, corrosion to NF, and lack of high temperature annealing
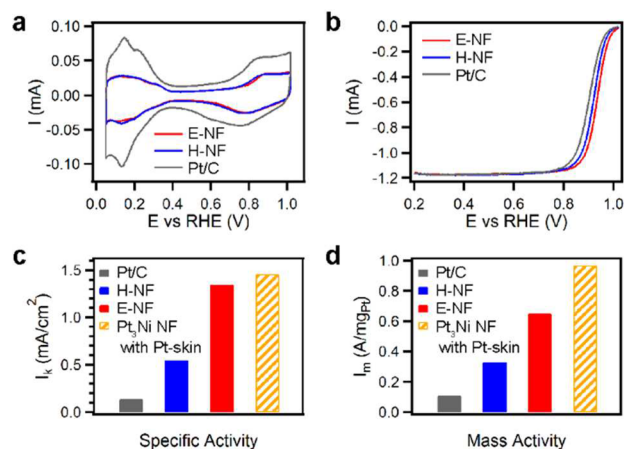
treatments, these NFs have Pt-skeleton surfaces (see SI for more details).[14] Future work will be dedicated to achieving Pt-skin surface formation on the quasi-2D E-NF in order to further optimize the surface structure.

A positive shift in the onset of hydroxyl adsorption of ∼18 mV occurred for E-NF versus that of H-NF, accompanied by a negative shift in the H_{upd}. This indicates weaker binding of surface species to E-NF, which is in agreement with increased near-surface Ni composition and fewer low-coordinated sites on the E-NF surface. Figure 4b shows the ORR polarization curves demonstrate an increase in activity along the following trend: Pt/C < H-NF < E-NF (also Figure S10). The calculated kinetic current density at 0.95 V versus the reversible hydrogen electrode (RHE) was normalized over the $ECSA_{Hupd}$ and Pt mass loading to give the specific and mass activity, respectively, and compared to the earlier study of Pt_3Ni NF with Pt-skin (Figure 4c,d). Of the catalysts studied in this work, E-NF exhibits the highest specific and mass activity, ∼10 and 6 times higher than that of commercial Pt/C, respectively. E-NF shows specific activity of 1.35 mA/cm², a 145% specific activity enhancement compared with H-NF (0.55 mA/cm²), and does not show any morphological change after electrochemical testing (Figure S11). The enhanced electrocatalytic performance of E-NF is attributed to its extended surfaces that are more enriched in Ni and have fewer low-coordinated sites than the surface of H-NF. Though the quasi-2D structure of E-NF does lower its ECSA, the thin nature of the sheets in E-NF allows it to maintain high mass activity, approximately twice that of H-NF. This study emphasizes the impact that control of the three-dimensional elemental distribution in alloy nanocrystals can have on the design of new architectures.

In conclusion, we successfully controlled the three-dimensional elemental distribution within Pt−Ni SD, leading to structural differentiation after Ni corrosion into either hollow or excavated NFs. The excavated NF exhibited Pt-rich sheets extending inward from Pt-rich edges, whereas the hollow NF had empty space inside Pt-rich edges. These differences resulted in remarkable ORR activity improvement for the excavated NF. This work revealed the clear relationship

between structural properties and electrochemical performance, such as the Ni content in the near-surface region and the existence of extended sheet structure. These design strategies can be implemented in various bimetallic nanocrystal catalysts for electrochemical or other catalytic applications.

ASSOCIATED CONTENT

ⓈSupporting Information

The Supporting Information is available free of charge on the ACS Publications website at DOI: 10.1021/jacs.7b05584.

> Experimental details, electrochemical data (PDF)
> Spatial distribution of extended sheet structure (AVI)
> Spatial distribution of extended sheet structure (AVI)

AUTHOR INFORMATION

Corresponding Authors

*vrstamenkovic@anl.gov
*p_yang@berkeley.edu

ORCID ⊙

Nigel Becknell: 0000-0001-7857-6841
Dohyung Kim: 0000-0003-0201-9082
Yi Yu: 0000-0003-4326-5992
Zhiqiang Niu: 0000-0002-9122-4880
Peidong Yang: 0000-0003-4799-1684

Present Address

∇School of Physical Science and Technology, ShanghaiTech University, Shanghai, 201210, China

Author Contributions

¶These authors contributed equally.

Notes

The authors declare no competing financial interest.

ACKNOWLEDGMENTS

REFERENCES

(1) Debe, M. K. *Nature* **2012**, *486*, 43.
(2) Seh, Z. W.; Kibsgaard, J.; Dickens, C. F.; Chorkendorff, I.; Norskov, J. K.; Jaramillo, T. F. *Science* **2017**, *355*, 146.
(3) Turner, J. A. *Science* **2004**, *305*, 972.
(4) Borup, R.; Meyers, J.; Pivovar, B.; Kim, Y. S.; Mukundan, R.; Garland, N.; Myers, D.; Wilson, M.; Garzon, F.; Wood, D.; Zelenay, P.; More, K.; Stroh, K.; Zawodzinski, T.; Boncella, J.; McGrath, J. E.; Inaba, M.; Miyatake, K.; Hori, M.; Ota, K.; Ogumi, Z.; Miyata, S.; Nishikata, A.; Siroma, Z.; Uchimoto, Y.; Yasuda, K.; Kimijima, K.; Iwashita, N. *Chem. Rev.* **2007**, *107*, 3904.
(5) Gasteiger, H. A.; Marković, N. M. *Science* **2009**, *324*, 48.
(6) Stamenkovic, V. R.; Mun, B. S.; Arenz, M.; Mayrhofer, K. J. J.; Lucas, C. A.; Wang, G. F.; Ross, P. N.; Markovic, N. M. *Nat. Mater.* **2007**, *6*, 241.
(7) Nørskov, J. K.; Rossmeisl, J.; Logadottir, A.; Lindqvist, L.; Kitchin, J. R.; Bligaard, T.; Jonsson, H. *J. Phys. Chem. B* **2004**, *108*, 17886.
(8) Chen, C.; Kang, Y.; Huo, Z.; Zhu, Z.; Huang, W.; Xin, H. L.; Snyder, J. D.; Li, D.; Herron, J. A.; Mavrikakis, M.; Chi, M.; More, K. L.; Li, Y.; Marković, N. M.; Somorjai, G. A.; Yang, P.; Stamenkovic, V. R. *Science* **2014**, *343*, 1339.
(9) Han, B.; Carlton, C. E.; Kongkanand, A.; Kukreja, R. S.; Theobald, B. R.; Gan, L.; O'Malley, R.; Strasser, P.; Wagner, F. T.; Shao-Horn, Y. *Energy Environ. Sci.* **2015**, *8*, 258.
(10) Wang, D. L.; Xin, H. L. L.; Hovden, R.; Wang, H. S.; Yu, Y. C.; Muller, D. A.; DiSalvo, F. J.; Abruna, H. D. *Nat. Mater.* **2013**, *12*, 81.
(11) Stamenkovic, V. R.; Fowler, B.; Mun, B. S.; Wang, G. F.; Ross, P. N.; Lucas, C. A.; Markovic, N. M. *Science* **2007**, *315*, 493.
(12) Wang, C.; Chi, M. F.; Li, D. G.; Strmcnik, D.; van der Vliet, D.; Wang, G. F.; Komanicky, V.; Chang, K. C.; Paulikas, A. P.; Tripkovic, D.; Pearson, J.; More, K. L.; Markovic, N. M.; Stamenkovic, V. R. *J. Am. Chem. Soc.* **2011**, *133*, 14396.
(13) Becknell, N.; Kang, Y.; Chen, C.; Resasco, J.; Kornienko, N.; Guo, J.; Markovic, N. M.; Somorjai, G. A.; Stamenkovic, V. R.; Yang, P. *J. Am. Chem. Soc.* **2015**, *137*, 15817.
(14) van der Vliet, D. F.; Wang, C.; Li, D.; Paulikas, A. P.; Greeley, J.; Rankin, R. B.; Strmcnik, D.; Tripkovic, D.; Markovic, N. M.; Stamenkovic, V. R. *Angew. Chem., Int. Ed.* **2012**, *51*, 3139.
(15) Niu, Z.; Becknell, N.; Yu, Y.; Kim, D.; Chen, C.; Kornienko, N.; Somorjai, G. A.; Yang, P. *Nat. Mater.* **2016**, *15*, 1188.
(16) Cui, C. H.; Gan, L.; Heggen, M.; Rudi, S.; Strasser, P. *Nat. Mater.* **2013**, *12*, 765.
(17) Gan, L.; Cui, C.; Heggen, M.; Dionigi, F.; Rudi, S.; Strasser, P. *Science* **2014**, *346*, 1502.
(18) Becknell, N.; Zheng, C.; Chen, C.; Yu, Y.; Yang, P. *Surf. Sci.* **2016**, *648*, 328.
(19) Jia, Y. Y.; Jiang, Y. Q.; Zhang, J. W.; Zhang, L.; Chen, Q. L.; Xie, Z. X.; Zheng, L. S. *J. Am. Chem. Soc.* **2014**, *136*, 3748.
(20) Hwang, B.-J.; Sarma, L. S.; Chen, J.-M.; Chen, C.-H.; Shih, S.-C.; Wang, G.-R.; Liu, D.-G.; Lee, J.-F.; Tang, M.-T. *J. Am. Chem. Soc.* **2005**, *127*, 11140.
(21) Stamenkovic, V.; Mun, B. S.; Mayrhofer, K. J. J.; Ross, P. N.; Markovic, N. M.; Rossmeisl, J.; Greeley, J.; Nørskov, J. K. *Angew. Chem., Int. Ed.* **2006**, *45*, 2897.
(22) Kitchin, J. R.; Nørskov, J. K.; Barteau, M. A.; Chen, J. G. *J. Chem. Phys.* **2004**, *120*, 10240.
(23) Wang, C.; van der Vliet, D.; Chang, K. C.; You, H. D.; Strmcnik, D.; Schlueter, J. A.; Markovic, N. M.; Stamenkovic, V. R. *J. Phys. Chem. C* **2009**, *113*, 19365.